ELSEVIER

Contents lists available at ScienceDirect

# International Journal of Greenhouse Gas Control

journal homepage: www.elsevier.com/locate/ijggc





# Surrogate model optimization of vacuum pressure swing adsorption using a flexible metal organic framework with hysteretic sigmoidal isotherms

Yuya Takakura <sup>a</sup>, Suryateja Ravutla <sup>b</sup>, Jinsu Kim <sup>c</sup>, Keisuke Ikeda <sup>a</sup>, Hiroshi Kajiro <sup>d</sup>, Tomoyuki Yajima <sup>a</sup>, Junpei Fujiki <sup>e</sup>, Fani Boukouvala <sup>b</sup>, Matthew Realff <sup>b</sup>, Yoshiaki Kawajiri <sup>a,f,\*</sup>

- <sup>a</sup> Materials Process Engineering, Nagoya University, Nagoya, Aichi 464-8603, Japan
- <sup>b</sup> School of Chemical and Biomolecular Engineering, Georgia Institute of Technology, Atlanta, GA 30332, USA
- <sup>c</sup> Department of Petrochemical Materials, Chonnam National University, 50 Daehak-ro, Yeosu-si, 59631, Republic of Korea
- d Nippon Steel Co., Advanced Technology Research Laboratories, Environmental Research Lab., 20-1 Shintomi, Futtsu, Chiba 293-8511, Japan
- e Research Center for Net Zero Carbon Society, Institutes for Innovation for Future Society, Nagoya University, Nagoya, Aichi 464-8603, Japan
- f School of Engineering Science, LUT University, Mukkulankatu 19, Lahti 15210, Finland

#### ARTICLE INFO

# Keywords: Carbon capture Surrogate model Process simulation and optimization Vacuum pressure swing adsorption (VPSA) Flexible metal-organic frameworks (MOFs)

#### ABSTRACT

This study presents a process optimization study for a vacuum pressure swing adsorption (VPSA) process using a flexible metal-organic framework (MOF), which is gaining attention as a material to realize energy-efficient carbon dioxide capture processes. Many flexible MOFs exhibit sigmoidal adsorption isotherms with hysteresis, posing a challenge for simulation and optimization using a rigorous process model. In this study, we employ surrogate model optimization, where surrogate models using machine-learning algorithms were constructed from simulation of 903 operating conditions generated by Latin hypercube sampling. The surrogate models with the best performance were identified from 18 different surrogate options considering four design variables—adsorption pressure, desorption pressure, adsorption time, and desorption time. Using the best surrogate models, a multi-objective optimization problem was solved to identify the Pareto front among recovery, energy consumption, and bed size factor. Our analysis identified a distinct characteristic of VPSA using a flexible-MOF where purity and recovery are hardly affected by the feed volume.

#### 1. Introduction

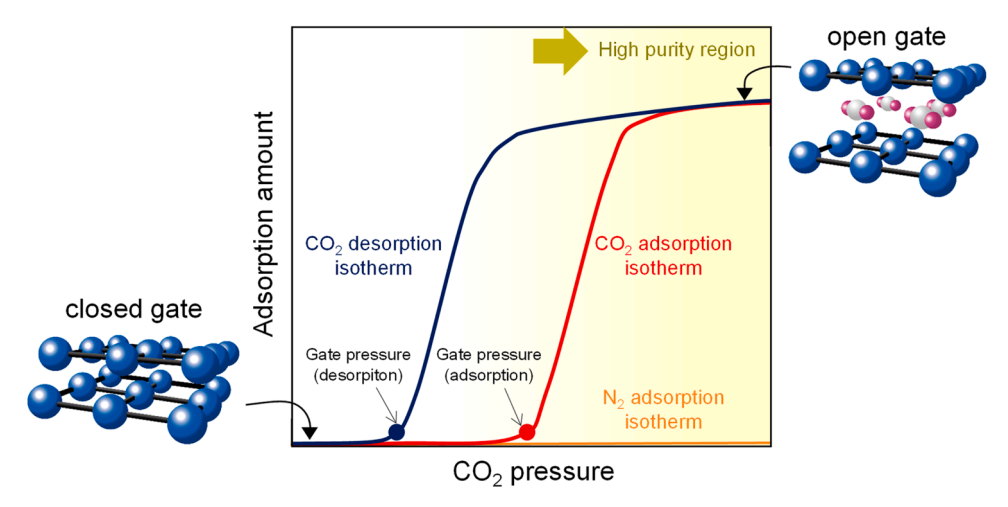
Carbon dioxide (CO<sub>2</sub>) emissions constitute a significant environmental concern due to their contribution to global warming. These emissions arise predominantly from industrial activities, with thermal power plants and manufacturing facilities being major point sources (Aaron and Tsouris, 2005). Capture of CO<sub>2</sub> from flue gas presents an essential technology in efforts to mitigate these emissions. To date, various methodologies for CO<sub>2</sub> capture, such as amine absorption, membrane separation, and cryogenic separation, have been proposed. Among these technologies, the vacuum pressure swing adsorption (VPSA) process is considered as particularly promising due to its potential for lower energy consumption (Shen et al., 2011).

Various kinds of adsorbents have been tested in VPSA processes. Historically, zeolites and activated carbons have been used in VPSA processes due to their high adsorption capacity and durability (Ko et al., 2005; Shen et al., 2012; Xu et al., 2019). Recently, metal-organic

frameworks (MOFs) for their highly tunable and customizable nature, have attracted considerable attention as potential adsorbents. Specifically, flexible MOFs have demonstrated promise for CO<sub>2</sub> capture owing to their unique "gate-opening/closing" property triggered by adsorption (Fig. 1) (Coudert et al., 2013; Horike et al., 2009; James, 2003; Majchrzak-Kucęba et al., 2019; Schneemann et al., 2014; Zhou and Kitagawa, 2014). This distinctive feature, giving rise to sigmoidal adsorption isotherms, achieves high working capacity and selectivity. In these isotherms, once the CO<sub>2</sub> pressure exceeds the "gate pressure", the amount of adsorption increases sharply. Flexible MOFs also exhibit intrinsic thermal management, where the exothermic heat generated during adsorption is counterbalanced by the endothermic expansion of the framework (Hiraide et al., 2017; Mason et al., 2015). Furthermore, isotherms of flexible MOFs often have hysteresis, where adsorption and desorption do not follow the same trajectory. These distinctive characteristics of flexible MOFs require special attention in mathematical modeling, as discussed below. Among the various flexible MOFs, Elastic Layer-structured Metal-organic Framework-11 (ELM-11) is particularly

<sup>\*</sup> Corresponding author at: Materials Process Engineering, Nagoya University, Nagoya, Aichi 464-8603, Japan. *E-mail address*: kawajiri@nagoya-u.jp (Y. Kawajiri).

Nomenclature		$n_{\text{switch}}$	amount of CO <sub>2</sub> adsorbed at switched point [molCO <sub>2</sub> /kg <sub>ads</sub> ] saturated amount of CO <sub>2</sub> adsorption at a temperature <i>T</i>
$b_{ m L}$	imaginary adsorption isotherm parameter for CO <sub>2</sub>	$n_{\rm sat}(T)$	[molCO <sub>2</sub> /kg <sub>ads</sub> ]
$ u_{\rm L}$	[molCO <sub>2</sub> /(kg <sub>ads</sub> ·kPa)]	n	partial pressure of CO <sub>2</sub> [kPa]
$b_{ m U}$	temperature dependent value for imaginary CO <sub>2</sub>	P <sub>CO2</sub>	target partial pressure of CO <sub>2</sub> during adsorption step [kPa]
υ	adsorption isotherm [kPa <sup>-1</sup> ]	$p_{ m CO2,tar} \ P_{ m des}$	desorption pressure [kPa]
$b_{ m U}^\infty$	imaginary adsorption isotherm parameter for CO <sub>2</sub> [kPa <sup>-1</sup> ]	$P_{\mathrm{feed}}$	feed gas pressure [kPa]
$b_{ m H}$	imaginary adsorption isotherm parameter for CO <sub>2</sub> [Ki a ]		T) foot CO <sub>2</sub> pressure at a temperature T for adsorption [kPa]
$\nu_{ m H}$	[molCO <sub>2</sub> /(kg <sub>ads</sub> ·kPa)]		T) foot CO <sub>2</sub> pressure at a temperature T for desorption [kPa]
$b_{ m N_2}$	adsorption isotherm parameter for $N_2$ [molN <sub>2</sub> /(kg <sub>ads</sub> ·kPa)]	product	
$C_{pg}$	heat capacity of gas [J/(kg·K)]	product	[molCO <sub>2</sub> ]
$C_{ps}$	heat capacity of solid [J/(kg·K)]	$q_i$	amount of component <i>i</i> adsorbed [mol/kg <sub>ads</sub> ]
$C_{ m ads}$	coefficient for adsorption time [-]	$q_i^*$	equilibrium amount of component <i>i</i> adsorbed [mol/kg <sub>ads</sub> ]
$C_{ m des}$	coefficient for desorption pressure [-]	q <sub>CO2,tar</sub>	target amount of CO <sub>2</sub> adsorbed during desorption step
$D_L$	axial dispersion coefficient [m <sup>2</sup> /s]	<b>4</b> CO2,tar	[molCO <sub>2</sub> /kg <sub>ads</sub> ]
$E_{\rm com}$	power consumption for the compressor [GJ <sub>e</sub> /tonne-CO <sub>2</sub> ]	R	gas constant [J/(mol·K)]
$E_{\mathrm{U}}$	imaginary adsorption isotherm parameter for CO <sub>2</sub> [kJ/	$t_{ m ads}$	adsorption time [s]
-0	molCO <sub>2</sub> ]	$t_{ m cycle}$	cycle time [s]
$E_{ m vac}$	power consumption for the vacuum pump [GJ <sub>e</sub> /tonne-	$t_{ m des}$	desorption time [s]
-vac	CO <sub>2</sub> ]	$t_{ m depress}$	depressurization time [s]
feed	amount of CO <sub>2</sub> feed gas [molCO <sub>2</sub> ]	$t_{ m des}$	desorption time [s]
h	heat transfer coefficient [J/(m²·s·K)]	$t_{\rm des}$	time needed until the amount of CO <sub>2</sub> adsorbed at the inlet
$H_{\mathrm{step},j}$	enthalpy of the phase transitions [kJ/molCO <sub>2</sub> ]		reaches the target value [s]
i	component	T	temperature [K]
impurity	•	$T_{ m feed}$	feed temperature [K]
j	mode of hysteretic isotherms	$T_{ m wall}$	column wall temperature [K]
$k_i$	overall mass transfer coefficient of component <i>i</i> [1/s]	и	gas velocity [m s <sup>-1</sup> ]
$K_L$	axial thermal conductivity [J/(m·s·K)]	$w_i$	weight [-]
L	column length [m]	$y_{i,\text{feed}}$	feed mole fraction of component <i>i</i> [-]
mode	binary variable for mode of hysteretic isotherms [-]	Z	axial position in column [m]
$n_{ m L}$	imaginary adsorption isotherm where the gate is always	$v_j$	weighting function parameter [-]
	closed [molCO <sub>2</sub> /kg <sub>ads</sub> ]	$\chi_j$	parameter for the weighting function $w_j$ [-]
$n_{ m U}$	imaginary adsorption isotherm where the gate is always	$\varepsilon_{\mathrm{bed}}$	bed void [-]
	open [molCO <sub>2</sub> /kg <sub>ads</sub> ]	$\eta_{\mathrm{com}}$	efficiency of compressor [-]
$n_j$	adsorption/desorption isotherms of CO <sub>2</sub> [mol/kg <sub>ads</sub> ]	$\eta_{ m vac}$	efficiency of vacuum pump [-]
$n_{\mathrm{U}}^{\infty}$	saturated amount of CO <sub>2</sub> adsorption [molCO <sub>2</sub> /kg <sub>ads</sub> ]	$ ho_{ m ads}$	adsorbent density without binder [kg <sub>ads</sub> /m <sup>3</sup> ]
$n_{\mathrm{des}  o \mathrm{ads}}$	secondary or higher-order adsorption isotherm [molCO <sub>2</sub> /	$ ho_{ m pellet}$	pellet density [kg/m³]
	kg <sub>ads</sub> ]	$ ho_{ m wall}$	wall density [kg/m³]
$n_{\mathrm{ads} \rightarrow \mathrm{des}}$	secondary or higher-order desorption isotherm [molCO <sub>2</sub> /	$\mu$	gas viscosity [kg/(m·s)]
	kg <sub>ads</sub> ]	γ	heat capacity ratio [-]
n <sub>sat</sub>	saturated amount of CO <sub>2</sub> adsorption [molCO <sub>2</sub> /kg <sub>ads</sub> ]		



 $\textbf{Fig. 1.} \ \ \textbf{Isotherm hysteresis with the gate-opening/closing property.}$ 

promising. As first reported by Li and Kaneko (2001), ELM-11 has superior CO<sub>2</sub> working capacity and selectivity, which have been extensively explored by many researchers (Bon et al., 2015; Kondo et al., 2006; Kultaeva et al., 2018; Tanaka et al., 2015; Yang et al., 2012).

Dynamic simulation of adsorption processes in flexible MOFs, characterized by sigmoidal isotherms and isotherm hysteresis, is a challenging task. Rigorous dynamic models, represented by partial differential algebraic equations (PDAEs), pose significant challenges due to nearly discrete and non-differentiable changes within the system. These challenges arise from the sigmoidal isotherm shapes and switching of isotherm trajectories caused by the hysteresis in flexible MOFs. Despite these difficulties, our team has successfully modeled the equilibrium and kinetics, and developed a dynamic simulation of the VPSA process with ELM-11 using advanced mathematical methods (Fujiki et al., 2023; Sugimoto et al., 2023; Takakura et al., 2022).

In the above dynamic simulation, the VPSA process using ELM-11 was analyzed in detail and compared with a conventional adsorbent zeolite 13X, reporting the following: (1) the ELM-11 isotherms for CO<sub>2</sub> at temperatures ranging from -10 °C to 25 °C and a N2 isotherm were measured (the isotherms and its fittings are shown in Supplementary Material (S.2)); (2) models were created from the isotherms data, showing different adsorption equilibrium states due to hysteresis in cyclic operation; (3) due to the large working capacity of CO<sub>2</sub> and the small amount of N2 adsorbed, the purity is above 98 % in all cases in the region where the feed CO2 pressure exceeds the gate pressure ("high purity region" in Fig. 1); (4) the CO<sub>2</sub> recovery rate was found to depend greatly on how much higher the feed CO2 pressure is compared to the gate pressure, requiring careful control of temperature and pressure; and (5) the validity of the adsorption rate equation was also examined. While this advancement enabled us to evaluate effective operations and assess process performance using ELM-11, optimization of the process using a rigorous dynamic model has yet to be addressed, which is an even more difficult computational challenge. The sigmoidal isotherms with hysteresis, which are implemented as a hybrid model (Barton and Pantelides, 1994; Peszyńska and Showalter, 1998) would not allow Newton-based optimization that requires computations of derivatives (gradients and Jacobians) of functions. Furthermore, attaining a cyclic-steady-state (CSS), for example, necessitates a sequence of repeated cyclic operations (Kim et al., 2022; Takakura et al., 2022). The computational demand is further exacerbated in optimization, which requires iterative computation for CSSs under different operating conditions.

In recent years, optimization using surrogate modeling has been reported for PSA processes. Several researchers have employed different surrogate modeling methods to address similar challenges (Table 1). For example, Kim et al. (2022) implemented various machine-learning methodologies using Pycaret, a versatile Python-based framework, for the separation of carbon monoxide from steel-mill off-gas, achieving a cost-effective operation. Agarwal et al. (2009) proposed a reduced-order

Table 1 Surrogate modeling studies for PSA processes.

Refs.	Separation process	Separation system
Kim et al. (2022)	Four-bed six-step VPSA	CO separation
Kim et al. (2022)	Four-step VPSA	CO <sub>2</sub> capture
Agarwal et al. (2009)	Two-bed four-step PSA	H <sub>2</sub> purification
Beck et al. (2015)	Two-bed six-step VPSA	Post-combustion CO2 capture
Sant Anna et al. (2017)	Single bed four-step PSA	N <sub>2</sub> rejection from natural gas
Ye et al. (2019)	Single bed four-step PSA	H <sub>2</sub> purification
Leperi et al. (2019)	Three to five step PSA	Post-combustion CO2 capture
Subraveti et al. (2019)	Four to ten step PSA	Post combustion CO2 capture
(Pai et al., 2020)	Two-bed four-step VPSA	Post-combustion CO2 capture
Xiao et al. (2020)	Two-bed six-step PSA	H <sub>2</sub> purification
Vo et al. (2020)	Two-bed six-step PSA	H <sub>2</sub> recovery and CO <sub>2</sub> capture
Hao et al. (2021)	Four-step PSA	CO <sub>2</sub> capture
Tong et al. (2021)	Two-bed six-step PSA	H <sub>2</sub> purification
Yu et al. (2021)	Four-bed six-step PSA	H <sub>2</sub> purification

model using proper orthogonal decomposition (POD) for hydrogen (H<sub>2</sub>) purification. Beck et al. (2015) adopted kriging regression for handling output uncertainty and demonstrated a comparable Pareto front. Artificial neural networks (ANNs) have been used in many studies, such as Sant Anna et al. (2017) for achieving target purity of nitrogen (N2), and Ye et al. (2019) for obtaining high-purity H<sub>2</sub> from multicomponent mixtures. Leperi et al. (2019) applied ANNs for CO<sub>2</sub> capture assessing PSA systems, while Subraveti et al. (2019) used partial least square (PLS) regression for surrogate model development. A variety of surrogate models developed by machine-learning algorithms, including ANN, have been used with a focus on CO2 capture systems, as reported by Pai et al. (2020). Xiao et al. (2020) compared ANN and polynomial regression surrogate models, emphasizing superior performance of ANN in H2 purification. Vo et al. (2020) achieved feasible H2 recovery and CO2 capture solutions using ANN optimizations and model order reduction via singular value decomposition (SVD). Kim et al. screened 75 adsorbent options using ANN regression (Kim et al., 2022). Furthermore, Hao et al. (2021) proposed a hybrid framework for PSA optimization using Gaussian process and gradient-based algorithm, while Tong et al. (2021) and Yu et al. (2021) used ANN for optimization of H<sub>2</sub> purification. Nevertheless, optimization of a PSA process using a flexible MOF has not been reported.

In this study, we analyze optimal operations of the VPSA process for CO2 capture using the flexible metal-organic framework ELM-11 for the first time, where the numerical challenges for the sigmoidal isotherms with hysteresis were resolved by a surrogate model optimization approach by machine learning. Utilizing Latin hypercube sampling (LHS), we generated a diverse dataset from 903 distinct operating conditions to construct reliable surrogate models. The predictability of the surrogate model was carefully validated, and the most reliable surrogate model was identified from 18 candidates of surrogate models. Using the surrogate model, multi-objective optimization was performed for four objective functions: recovery, bed size factor (BSF), power consumption, and purity. The solution of the optimization problem, a fourdimensional Pareto front, allows us to analyze the trade-off of the four objective functions. Our analysis identifies unique characteristics of adsorption processes using flexible MOFs which cannot be seen in those using conventional adsorbents.

## 2. Process descriptions and analysis

#### 2.1. Isotherm modeling

ELM-11 exhibits complex hysteresis behavior, causing shifts in the isotherm trajectory between adsorption and desorption. This results in infinite variations of isotherm trajectories influenced by the historical cycles of adsorption and desorption, significantly complicating the analysis of the adsorption process.

Our previous work classified the infinite patterns of adsorption/desorption isotherm exhibited by ELM-11 into four main categories (Takakura et al., 2022), as shown in Fig. 2(a). The *primary* isotherm for adsorption, shown as (I) in the figure, is generated from the origin, or a clean state, with monotonically increasing CO<sub>2</sub> pressure. Similarly, the primary isotherm for desorption, shown as (II) in the figure, is generated from a saturated state with monotonically decreasing CO<sub>2</sub> pressure.

The trajectories shown as (III) and (IV) in Fig. 2(a), are the *secondary* isotherms, categorized as generated when a switch occurs between adsorption and desorption at an intermediary point between the clean and saturated states. For example, in the secondary isotherm (III), adsorption is carried out from the origin until reaching the light-blue circle, and then desorption is carried out. Similarly in the secondary isotherm (IV), desorption is carried out from the saturated state until reaching the orange circle, and then adsorption is carried out. Moreover, when switching between adsorption/desorption is repeated on the trajectories of second-order isotherms, the isotherm follows an even higher-order trajectory. Thus, the equilibrium depends on the history of

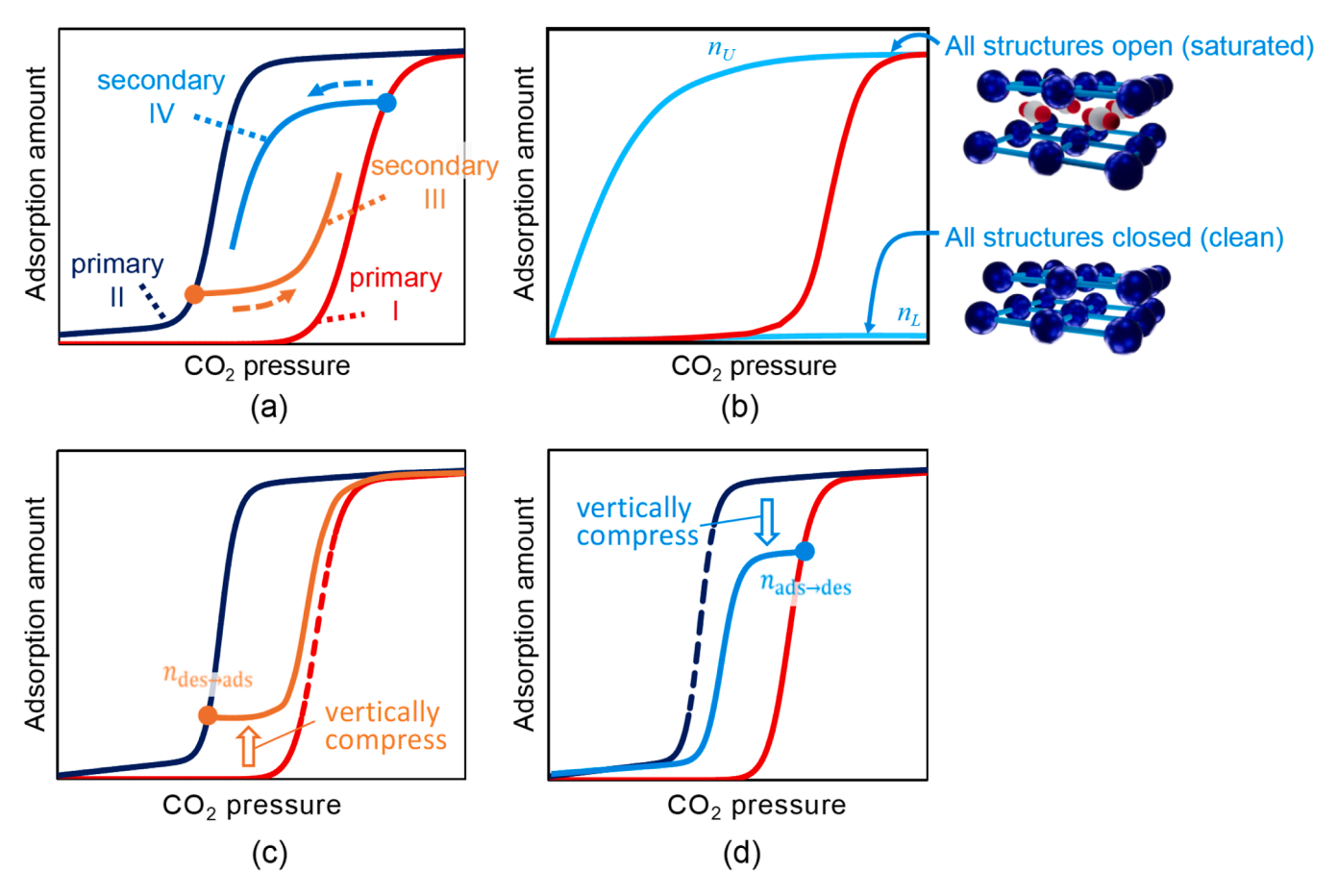


Fig. 2. Adsorption and desorption isotherms of ELM-11: (a) hysteresis given by primary and secondary isotherms; (b) modeling approach for sigmoidal isotherm using imaginary isotherms; (c) modeling of a secondary adsorption isotherm; and (d) modeling of a secondary desorption isotherm.

switching between adsorption and desorption, and there exists an infinite number of isotherm trajectories for hysteretic adsorbents.

For the primary isotherms, the sigmoidal shape is modeled using the approach proposed by Hefti et al. (2016) which have been validated in our previous studies (Fujiki et al., 2023; Sugimoto et al., 2023; Takakura et al., 2022). We consider imaginary adsorption isotherms in Fig. 2(b). There, the lower isotherm  $n_{\rm L}$  is an *imaginary* adsorption isotherm where the structures always remain closed regardless of the CO<sub>2</sub> partial pressure. On the other hand, the upper isotherm  $n_{\rm U}$  is another imaginary isotherm where the structures remain open, and the molecules can enter the internal space. We consider the weighted sum of uptakes given by these two imaginary isotherms:

$$n_j = n_U w_j + n_L (1 - w_j), \ j \in (ads, des). \tag{1}$$

where *j* is mode of isotherms (adsorption and desorption), and  $w_j \in [0, 1]$  is the weight. The imaginary isotherms  $n_L$  and  $n_U$  are given by:

$$n_{\rm L} = b_{\rm L} p_{\rm CO_2}, \tag{2}$$

$$n_{\rm U} = \frac{n_{\rm U}^{\infty} b_{\rm U} p_{\rm CO_2}}{1 + b_{\rm U} p_{\rm CO_2}} + b_{\rm H} p_{\rm CO_2},\tag{3}$$

$$b_{\rm U} = b_{\rm U}^{\infty} \exp\left(\frac{E_{\rm U}}{RT}\right),\tag{4}$$

where  $b_{\rm L}$ ,  $b_{\rm U}^{\infty}$ ,  $b_{\rm H}$ , and  $E_{\rm U}$  are parameters for the imaginary adsorption isotherms;  $p_{\rm CO_2}$  is partial pressure of CO<sub>2</sub>; T is temperature. The weight  $w_i$  is modeled as follows:

$$w_{j} = \frac{\exp\left(\frac{\ln\left(p_{\text{CO}_{2}}\right) - \ln\left(p_{\text{step},j}(T)\right)}{\chi_{j}}\right)}{1 + \exp\left(\frac{\ln\left(p_{\text{CO}_{2}}\right) - \ln\left(p_{\text{step},j}(T)\right)}{\chi_{j}}\right)},\tag{5}$$

where  $\chi_j$  is a parameter for the weight;  $p_{\text{step},j}(T)$  is the step pressure of isotherm j at temperature T. The step pressure is modeled as follows:

$$p_{\text{step},j}(T) = p_{\text{step}0,j} \exp\left(-\frac{H_{\text{step},j}}{R} \left(\frac{1}{T_0} - \frac{1}{T}\right)\right), \tag{6}$$

where  $p_{\text{step0,}j}$  is the step pressure of isotherm j at  $T_0 = 273.15$  [K]; and  $H_{\text{step,}j}$  is the enthalpy of the phase transition.

The secondary isotherms are given by *vertically compressing* the primary isotherms. The equilibrium follows the branched trajectory  $n_{\text{des} \to \text{ads}}$  shown as the orange line in Fig. 2(c) when desorption is carried out from the saturated state until reaching orange circle, and then adsorption occurs. We obtain the secondary isotherm  $n_{\text{des} \to \text{ads}}$  by vertically compressing the primary isotherm  $n_{\text{ads}}$  from the bottom to the top as follows:

$$n_{\text{des}\to\text{ads}} = n_{\text{ads}} \cdot \left\{ \frac{(n_{\text{sat}} - n_{\text{switch}})}{n_{\text{sat}}} \right\} + n_{\text{switch}}, \tag{7}$$

where  $n_{\rm switch}$  is the amount of CO<sub>2</sub> adsorbed at the time of the switch between adsorption and desorption;  $n_{\rm sat}$  is a saturated amount of CO<sub>2</sub> uptake. Similarly, the equilibrium follows the trajectory  $n_{\rm ads \rightarrow des}$  shown as a light-blue line in Fig. 2(d), where adsorption is carried out from the clean state until reaching the light blue circle, and then desorption is carried out. The secondary isotherm can be modeled similarly by

vertically compressing the primary isotherm  $n_{\text{des}}$ , but this time *from the top to the bottom*, as follows:

$$n_{\mathrm{ads} \to \mathrm{des}} = n_{\mathrm{des}} \cdot \left(\frac{n_{\mathrm{switch}}}{n_{\mathrm{sat}}}\right).$$
 (8)

Finally, the equilibrium amount of adsorption  $q_{\mathrm{CO}_2}^{*}$  is given by:

$$q_{\text{CO}_2}^* = n_{\text{des} \rightarrow \text{ads}} \cdot \text{mode} + n_{\text{ads} \rightarrow \text{des}} \cdot (1 - \text{mode}), \tag{9}$$

where mode is a binary variable. Here,  $q_{\mathrm{CO_2}}^*$  is equal to the adsorption isotherm  $n_{\mathrm{des} \to \mathrm{ads}}$  when mode = 1, and the desorption isotherm  $n_{\mathrm{ads} \to \mathrm{des}}$  when mode = 0. The variable mode takes the value of 1 only in the steps where the adsorption operation in a VPSA process is carried out:

$$\label{eq:mode} \begin{aligned} \text{mode} &= \begin{cases} 1 & \text{if } 0 \leq t < t_{\text{press}} + t_{\text{ads}} \\ 0 & \text{if } t_{\text{press}} + t_{\text{ads}} \leq t < t_{\text{press}} + t_{\text{ads}} + t_{\text{depress}} + t_{\text{des}} \end{cases}, \end{aligned} \tag{10}$$

where  $t_{\rm press}$ ,  $t_{\rm ads}$ ,  $t_{\rm depress}$ , and  $t_{\rm des}$  are pressurization, adsorption, depressurization, and desorption times, as shown in Section 2.1. The adsorption isotherm of  $N_2$  is approximated by the following linear model without temperature dependence:

$$q_{N_2}^* = b_{N_2} p_{N_2}, (11)$$

where  $b_{\rm N_2}$  is a parameter;  $q_{\rm N_2}^*$  is the equilibrium uptake of N<sub>2</sub>; and  $p_{\rm N_2}$  is partial pressure of N<sub>2</sub>.

#### 2.2. VPSA process model

This study considers a four-step VPSA process shown in Fig. 3. This process configuration without rinse and purge steps was designed due to the intrinsic adsorption property of ELM-11, which has nearly zero  $\rm CO_2$  adsorption capacity at low pressures, as illustrated in Fig. 2(b). This unique property allows for the omission of rinse or purge steps often necessary in VPSA processes with conventional adsorbents (Takakura et al., 2022). By reducing the process to the four simple steps, we anticipate significant benefits, including shortening of cycle times and preventing purity drop of recovered  $\rm CO_2$ . Operating conditions including the feed  $\rm CO_2$  concentration are shown in the Supplementary Material (S.5).

In this process, the column is enveloped by a jacket maintained at a temperature of  $T_{\rm wall}$  [K], which is assumed to be equal to feed temperature  $T_{\rm feed}$  [K]. Note that the energy required for cooling is not considered in this study due to the difficulty in estimating it accurately. Furthermore, since the heat of adsorption for ELM-11 is low (Hiraide et al. 2017) the cooling cost would be relatively small. This process

undergoes the following cyclical steps until a cyclic steady state is achieved:

**Step 1 Pressurization:** A gas mixture of  $CO_2$  and  $N_2$  is introduced from the bottom inlet of the column until the desired pressure is achieved. During this stage, the top outlet of the column remains closed.

**Step 2 Adsorption:** The gas mixture continues to be fed from the inlet, while the outlet is opened to vent nitrogen-rich gas, thereby allowing  $CO_2$  adsorption onto the adsorbent in the column.

**Step 3 Depressurization**: The outlet is closed, and the column is depressurized to atmospheric pressure, preparing the system for the subsequent desorption step.

**Step 4 Desorption:** The column pressure is further reduced using a vacuum pump, which results in the desorption and collection of  ${\rm CO_2}$  product from the bottom of the column.

This study aims to optimize this simple four-step VPSA process by exploiting the unique CO<sub>2</sub> adsorption attributes of ELM-11, leading to the development of a high-performance CO<sub>2</sub> capture system.

In a typical VPSA process,  $CO_2$  is recovered from the outlet to prevent  $N_2$  contamination. However, in this process,  $CO_2$  is recovered from the inlet due to the high selectivity of ELM-11, which results in almost no  $N_2$  contamination when recovering  $CO_2$  from the feed inlet. Additionally, the sigmoidal desorption isotherm causes fast  $CO_2$  desorption which increases the gas which increases the gas  $CO_2$  concentration sharply during desorption, which would lead to a larger amount of  $CO_2$  readsorption if the product was recovered from the opposite end. By recovering  $CO_2$  from the feed inlet, this process effectively prevents readsorption and pressure loss, offering significant advantages.

The Partial Differential Algebraic Equation (PDAE) model is shown in Table 2. Boundary conditions and design parameters used in this study are presented in Section S.1 in the Supplementary Material. Further descriptions on the model can be found in the literature (Takakura et al., 2022).

#### 2.2. Performance indicators

To evaluate the efficiency of the process design and operation, four performance indicators are defined as shown in Table 2. These indicators have been widely utilized in some past studies (Bon et al., 2014; Hiraide et al., 2020, 2016; Kim et al., 2022; Takakura et al., 2022). Two commonly utilized metrics, purity and recovery, were selected to ascertain the influence of operating variables, such as operating pressure and temperature, on the overall effectiveness of the process. Details on these four performance indicators are shown in the Supplementary Material (S.4).

The four performance indicators in Table 3 are defined as follows:

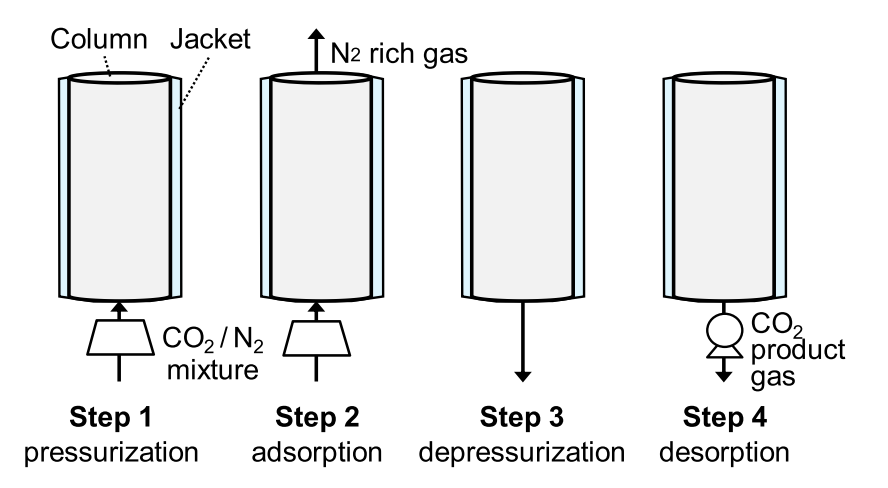


Fig. 3. Four-step cycle of the VPSA process.

**Table 2**Model equations for the VPSA simulation.

Component mass balance	$-  D_L iggl[ rac{\partial^2 y_i}{\partial z^2} + 2T iggl( rac{\partial y_i}{\partial z} iggr) iggl\{ rac{\partial}{\partial z} iggl( rac{1}{T} iggr) iggr\}  +$	(12)
	$2igg(rac{1}{P}igg)igg(rac{\partial y_i}{\partial z}igg)igg(rac{\partial P}{\partial z}igg)igg]$	
	$+rac{\partial y_i}{\partial t}+urac{\partial y_i}{\partial z}+rac{1}{arepsilon_{ ext{bed}}}rac{RT}{P} ho_{ ext{ads}}igg(rac{\partial q_i}{\partial t}-y_i{\sum}_irac{\partial q_i}{\partial t}igg)=0$	
Overall mass balance	$\frac{\partial u}{\partial z} + \frac{u}{P} \frac{\partial P}{\partial z} + uT \frac{\partial}{\partial z} \left(\frac{1}{T}\right) + T \frac{\partial}{\partial t} \left(\frac{1}{T}\right) + \frac{1}{P} \frac{\partial P}{\partial t}$	(13)
	$-D_Ligg[Trac{\partial^2}{\partial z^2}igg(rac{1}{T}igg)+rac{1}{P}rac{\partial^2 P}{\partial z^2}+$	
	$2igg(rac{T}{P}igg)igg(rac{\partial P}{\partial z}igg)igg(rac{\partial}{\partial z}igg(rac{1}{T}igg)igg) igg]$	
	$+rac{1}{arepsilon_{ m bed}}rac{RT}{P} ho_{ m ads}{\sum_i}rac{\partial q_i}{\partial t}=0$	
Ergun equation	$-\frac{\partial P}{\partial z} = 150 \frac{\mu u}{4R_p^2} \frac{\left(1 - \varepsilon_{\rm bed}\right)^2}{\varepsilon_{\rm bed}^3} +$	(14)
	$1.75 \frac{(1-\varepsilon_{\rm bed})}{2R_p \varepsilon_{\rm bed}^3} u  u  \rho_{\rm gas}$	
LDF model	$rac{\partial q_i}{\partial t} = k_i (q_i^* - q_i)$	(15)
Heat balance equation	$\left\{arepsilon_{ m bed} ho_{ m gas}C_{pg}+ ho_{ m pellet}C_{ps} ight\}rac{\partial T}{\partial t}+ ho_{ m gas}C_{pg}arepsilon_{ m bed}urac{\partial T}{\partial z}-$	(16)
	$K_L \frac{\partial^2 T}{\partial z^2}$	
	$-\rho_{\rm ads} \sum_{i} H_{i} \frac{\partial q_{i}}{\partial t} + \frac{2h}{R_{\rm bed}} (T - T_{\rm wall}) = 0$	

**Purity:** This metric represents the quality of the captured  $CO_2$ . A high purity indicates a greater concentration of  $CO_2$  in the product gas, improving the usability of the captured gas for downstream applications.

**Recovery:** This index reflects the proportion of  $CO_2$  successfully extracted from the feed. A higher recovery implies effective removal of  $CO_2$  from the gas mixture.

The remaining performance indicators, Bed Size Factor (BSF) and Power Consumption, pertain more directly to the operational efficiency and environmental and economic impact of the process.

**Bed Size Factor (BSF):** This index is measured in  $kg_{ads}$ /TPDCO<sub>2</sub>, where TPDCO<sub>2</sub> represents tonnes per day CO<sub>2</sub>. BSF is the amount of adsorbent needed to recover a tonne of CO<sub>2</sub> in one day. A lower BSF indicates a more economically efficient process, as less adsorbent material is needed to capture a given amount of CO<sub>2</sub> per unit time.

**Power Consumption:** Expressed in  $GJ_e$ /tonne- $CO_2$ , this performance indicator quantifies the amount of electrical energy required for compression and vacuum operations per unit weight of  $CO_2$  recovered. Importantly, it considers the efficiencies of the compressor  $\eta_{com}$  and that of the vacuum pump  $\eta_{vac}$ , with a particular emphasis on the fact that  $\eta_{vac}$  varies in response to changes in desorption pressure (Section S4 in the Supplementary Material). A lower value of power consumption indicates a more sustainable and economically efficient process.

#### 3. Methods

#### 3.1. Surrogate modeling

#### 3.1.1. Decision variables

The surrogate model in this study analyzes the influences of four decision variables, which are operating conditions for the PVSA operation. The decision variables are feed pressure  $P_{\rm feed}$  [kPa], column wall temperature  $T_{\rm wall}$  [K], coefficient for adsorption time  $C_{\rm ads}$  [-] which increases the adsorption time while the feed flow rate is set constant, and coefficient for desorption pressure  $C_{\rm des}$  [-] which are defined later. The learning datasets were obtained from variable ranges shown in Table 4. The ranges of  $P_{\rm feed}$  [kPa] and  $T_{\rm wall}$  [K] were chosen from adsorption and desorption isotherms of ELM-11. The ranges of  $C_{\rm ads}$  [-] and  $C_{\rm des}$  [-] were chosen to be sufficiently wide.

One of the decision variables  $C_{\rm ads}$  [-] is for choosing the optimal adsorption time. In the VPSA process operation, the adsorption time is terminated when the outlet  $CO_2$  pressure reaches a threshold value  $p_{CO2}$ ,  $t_{\rm at}$  [kPa] (see Fig. 4(a)):

$$p_{\text{CO}_2,\text{tar}} = C_{\text{ads}} \cdot p_{\text{foot,ads}}(T_{\text{wall}})$$
(17)

where  $p_{\text{foot,ads}}(T_{\text{wall}})$  [kPa] is the *foot CO<sub>2</sub> pressure* at which equilibrium CO<sub>2</sub> adsorption amount reaches 2 % of saturation at the column wall temperature  $T_{\text{wall}}$  [K] (see Fig. 4(b)):

$$p_{\text{foot,ads}}(T_{\text{wall}}) = 0.02 \cdot n_{\text{sat}}(T_{\text{wall}}), \tag{18}$$

where  $n_{\rm sat}(T_{\rm wall})$  [molCO<sub>2</sub>/kg<sub>ads</sub>] is the saturated amount of CO<sub>2</sub> adsorption at  $T_{\rm wall}$  [K]. This method of determining the adsorption time is based on the sigmoidal adsorption isotherm of ELM-11; it is observed that fast breakthrough of CO<sub>2</sub> begins when the CO<sub>2</sub> partial pressure at the outlet reaches 1.00-1.75 times the  $p_{\rm foot,ads}(T_{\rm wall})$  [kPa], which is represented by the value of  $C_{\rm ads}$  in Table 4.

Another decision variable  $C_{\text{des}}$  [-] is for choosing the optimal desorption pressure  $P_{\text{des}}$  [kPa] (see Fig. 4(c)):

$$P_{\text{des}} = C_{\text{des}} \cdot p_{\text{foot,des}}(T_{\text{wall}}). \tag{19}$$

where  $p_{\rm foot,des}(T_{\rm wall})$  [kPa] is the foot CO<sub>2</sub> pressure at which the equilibrium CO<sub>2</sub> desorption amount reaches 2 % of saturation at column wall temperature  $T_{\rm wall}$  [K] (see Fig. 4(b)). The range of  $C_{\rm des}$  [-], 0.20 – 0.70, was set after running some simulation trials to choose the conditions that give reasonable values of power consumption and desorption efficiency. Here, we found that a too short desorption time leads to unstable simulation. To enable computational convergence of the PDAEs, the desorption time  $t_{\rm des}$  [s] is determined by the following equation:

**Table 4**The four decision variables and search ranges.

Variables	Ranges
Feed Pressure $P_{\text{feed}}$ [kPa]	500 – 1500
Feed temperature $T_{\text{wall}}$ [K]	273.15 - 298.15
Coefficient for adsorption time $C_{ads}$ [-]	1.0 - 1.75
Coefficient for desorption pressure $C_{\text{des}}$ [-]	0.20 - 0.75

**Table 3** Four performance indicators.

Index	Definition	Unit
Recovery	Amount of CO <sub>2</sub> in product per cycle	%
	Amount of CO <sub>2</sub> in feed per cycle	
Purity	Amount of CO <sub>2</sub> in product per cycle	%
	Amount of CO <sub>2</sub> and inpurity in product per cycle	
BSF	Mass of adsorbent	kg <sub>ads</sub> /TPDCO <sub>2</sub>
	Amount of CO <sub>2</sub> in product per cycle / $t_{\rm cycle} \times 3600 \times 24$	
Power consumption	$\eta_{ m com} E_{ m com} + \eta_{ m vac} E_{ m vac}$	GJ <sub>e</sub> /tonne-CO <sub>2</sub>

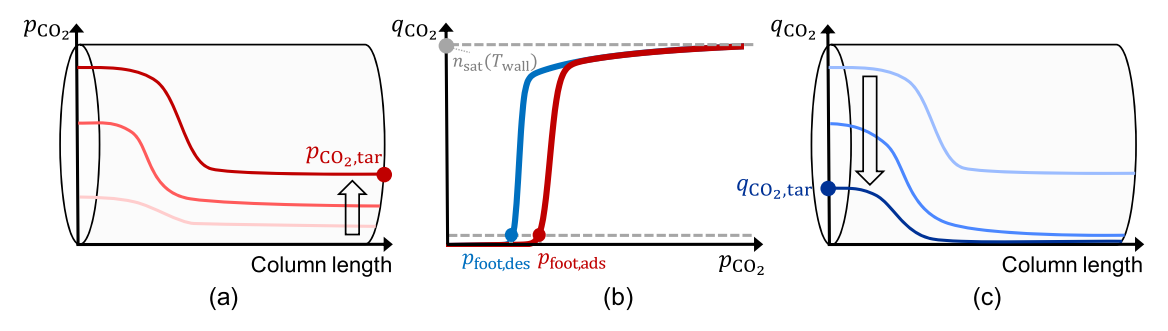


Fig. 4. Operation methods of the VPSA process: (a) CO<sub>2</sub> partial pressure at the outlet approaching  $p_{\text{CO2,tar}}$ ; (b) definition of  $p_{\text{foot,ads}}$ ,  $p_{\text{foot,des}}$ , and  $n_{\text{sat}}(T_{\text{wall}})$ ; and (c) amount of CO<sub>2</sub> adsorbed at the inlet approaching  $q_{\text{CO2,tar}}$ .

$$t_{\text{des}} = \max(t_{\text{des}}, 150),$$
 (20)

where  $t_{\text{des}}$ ' [s] is the time when the following condition is met, where the amount of CO<sub>2</sub> adsorbed at the inlet reaches  $q_{\text{CO2,tar}}$  [molCO<sub>2</sub>/kg<sub>ads</sub>]:

$$q_{\text{CO}_2,\text{tar}} = 0.30 \cdot n_{\text{sat}}(T_{\text{wall}}). \tag{21}$$

In Eqs. (20)-(21), the desorption time was set to be at least  $150 \, \mathrm{s}$  to avoid numerical difficulties. The vacuum operation is relatively time-consuming, and we believe enforcing a lower bound of  $150 \, \mathrm{s}$ , which is relatively short compared to the cycle time of approximately  $600 \, \mathrm{s}$ , is a reasonable assumption.

#### 3.1.2. Data generation for machine-learning

A total of 1511 points were collected for the ranges of the decision variables shown in Table 4. From the collected data, 608 points, in the range of  $P_{\rm feed} = 500$ –700 kPa and  $C_{\rm des} = 0.70$ –0.75, which gave unsatisfactory performance indicators, were eliminated a priori, resulting in 903 points to be used by the surrogate models. These sample points were determined by Latin hypercube sampling (LHS), which generate samples from a multidimensional domain, ensuring a more uniform coverage compared to simple random sampling (Kim et al., 2022). It divides each dimension into equispaced intervals and randomly selects one point from each interval, creating a set of stratified samples. LHS offers the

advantage of achieving sufficient accuracy with a smaller number of samples compared to other sampling techniques (Diwekar and Kalagnanam, 1997).

#### 3.1.3. Surrogate models

In this study, multiple surrogate models were constructed utilizing the PyCaret library (Hao et al., 2021). PyCaret is an open-source library for automated machine learning (AutoML) in Python that offers automation and simplification of processes from data preprocessing to model building, evaluation, and tuning. Various predictive modeling methodologies were employed using this library, including linear regression, tree-based algorithms such as decision trees and random forests, gradient-based algorithms such as XGBoost and LightGBM, and polynomial projection. These models provide a range of complexity and flexibility, suitable for different types of data and prediction tasks. We opted to use the default hyperparameters in PyCaret, which are derived from extensive empirical testing and optimization across a wide range of datasets and scenarios. This approach leverages the general applicability of these parameters, avoiding the potential overfitting that can result from extensive hyperparameter tuning. To avoid potential data bias and ensure the reliability of the model, a 10-fold cross-validation was conducted. The collected data points were partitioned into a 70 % training set, which was used to build the model, and a 30 % validation set, which

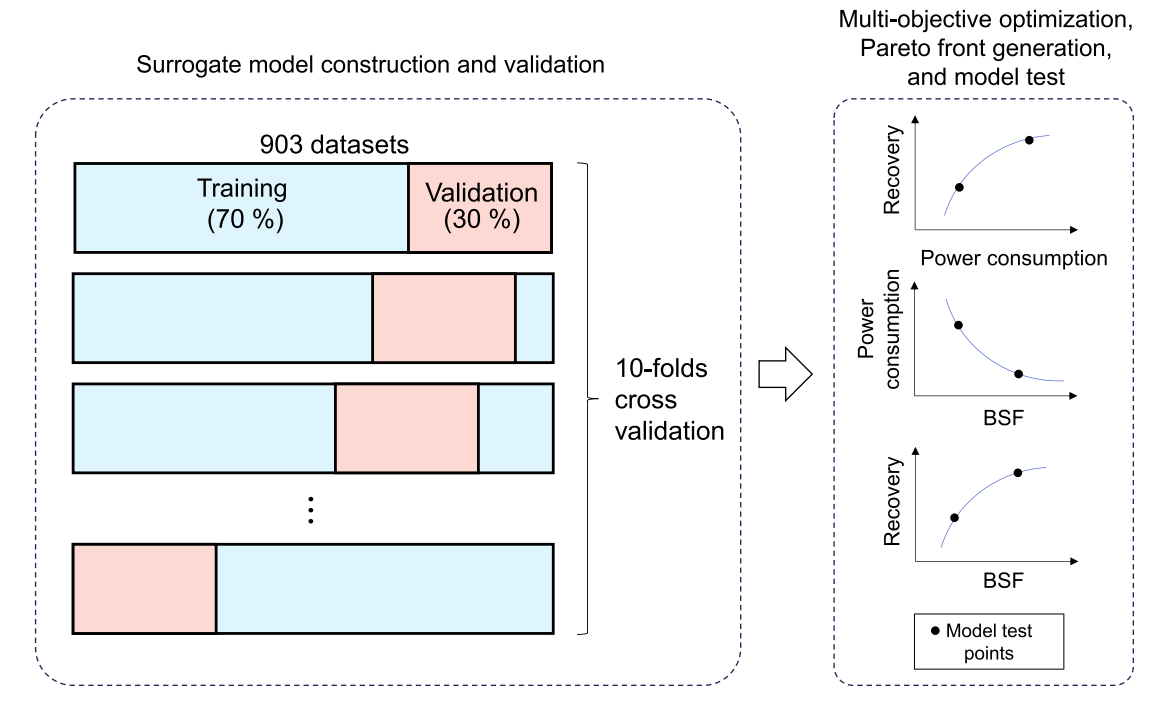


Fig. 5. Surrogate model construction, validation, multi-objective optimization, and test.

was employed to test the predictive accuracy of the models. The above procedure was repeated 10 times shifting the division between the training and validation sets (Fig. 5). Finally, the predictability of the surrogate models was tested by comparing the performance indicators with the rigorous models at four points on the parent front.

#### 3.2. Multi-objective optimization

Recovery of CO<sub>2</sub> [%]

Algorithm

To identify optimal operating conditions, the following multiobjective optimization problem was solved.

It should be noted that the purity was omitted from the objective function and constraint equations, as it consistently exceeded 98 % across all the 903 samples. This high purity is due to the very high  $CO_2/N_2$  selectivity of ELM-11. Even when we attempted to lower the feed pressure down to 500 kPa, purity remained above 98 % in every case. The optimization procedure was implemented within the Python 3.7.9 environment using the Optuna library (Akiba et al., 2019). The reproducibility of the optimization was ensured using the Tree-Structured Parzen Estimator (TPE) algorithm. The TPE algorithm is a form of Bayesian optimization designed for efficient optimization of model

MAE

hyperparameters. Specifically, it utilizes the results of past trials to suggest new parameter combinations to maximize model performance. Through iterative model building and evaluation, the algorithm progressively identifies the optimal set of hyperparameters (Lundberg et al., 2020).

#### 4. Results

#### 4.1. Algorithm selection and validation

Power consumption [GJe/tonne-CO2]

Algorithm

By using Pycaret, the most suitable surrogate model developed by machine learning algorithms was selected considering prediction accuracy. First, the training accuracy of the algorithms was evaluated using mean absolute error (MAE), mean squared error (MSE), root mean squared error (RMSE), and coefficient of determination (R²) (Table 5(a) and (b)). These metrics represent the average results from the ten crossfold-validation training runs. These metrics show a very similar trend across the multiple surrogate models, and in this study, the models with the highest R² values were chosen for further optimization. The Gradient Boosting Regressor algorithm was chosen for recovery, purity, and BSF, while the Extra Tree Regressor algorithm was chosen for power consumption.

Fig. 6 presents parity plots of the predicted results from the surrogate models and simulation results for the four performance indicators. These

MAE

MSE

 $R^2$ 

RMSE

**Table 5**Comparison of 18 surrogate models: (a) recovery and power consumption, (b) purity and BSF.

MSE

Gradient Boosting Regressor	0.7629	1.224	1.096	0.9798	Extra Trees Regressor	0.0301	0.0029	0.0516	0.9771
Extra Trees Regressor	0.7303	1.299	1.117	0.9790	Light Gradient Boosting Machine	0.0337	0.003	0.0533	0.9762
Light Gradient Boosting Machine	0.7327	1.326	1.134	0.9784	Gradient Boosting Regressor	0.0369	0.003	0.0538	0.9761
Random Forest Regressor	0.9767	1.798	1.331	0.9701	Random Forest Regressor	0.0383	0.0034	0.0571	0.9726
K Neighbors Regressor	1.355	3.693	1.906	0.9388	K Neighbors Regressor	0.0579	0.0076	0.0856	0.9402
Decision Tree Regressor	1.639	5.226	2.270	0.9109	Decision Tree Regressor	0.06300	0.0083	0.0901	0.9336
AdaBoost Regressor	2.034	6.362	2.507	0.8933	AdaBoost Regressor	0.0835	0.0115	0.107	0.9073
Least Angle Regression	1.987	7.580	2.739	0.8730	Least Angle Regression	0.0932	0.0179	0.1324	0.8563
Bayesian Ridge	1.986	7.580	2.739	0.8730	Bayesian Ridge	0.0932	0.0179	0.1324	0.8563
Ridge Regression	1.985	7.580	2.739	0.8730	Ridge Regression	0.0932	0.0179	0.1324	0.8563
Linear Regression	1.987	7.580	2.739	0.8730	Linear Regression	0.0932	0.0179	0.1324	0.8563
Huber Regressor	1.951	7.744	2.765	0.8712	Huber Regressor	0.0885	0.0189	0.1358	0.8489
Lasso Regression	2.323	11.10	3.305	0.8167	Passive Aggressive Regressor	0.1078	0.0229	0.1494	0.8172
Passive Aggressive Regressor	2.712	13.75	3.672	0.7603	Orthogonal Matching Pursuit	0.1995	0.0575	0.2395	0.538
Elastic Net	3.177	17.80	4.212	0.7034	Lasso Regression	0.2881	0.1279	0.3572	-0.022
Orthogonal Matching Pursuit	3.930	28.77	5.352	0.5157	Elastic Net	0.2881	0.1279	0.3572	-0.022
Lasso Least Angle Regression	6.245	61.60	7.822	-0.0266	Lasso Least Angle Regression	0.2881	0.1279	0.3572	-0.022
Dummy Regressor	6.245	61.60	7.822	-0.0266	Dummy Regressor	0.2881	0.1279	0.3572	-0.022
(b)									
Purity of product CO <sub>2</sub> [%]		BSF [kg <sub>ads</sub> /TPDCO <sub>2</sub> ]							
Algorithm	MAE	MSE	RMSE	R <sup>2</sup>	Algorithm	MAE	MSE	RMSE	$R^2$
Gradient Boosting Regressor	0.0427	0.0066	0.0796	0.9099	Gradient Boosting Regressor	33.57	4285	62.20	0.9729
Extra Trees Regressor	0.0406	0.0072	0.0818	0.9069	Light Gradient Boosting Machine	31.71	4490	63.82	0.9715
Light Gradient Boosting Machine	0.0425	0.0075	0.0839	0.8982	Extra Trees Regressor	31.10	5006	65.46	0.9686
Random Forest Regressor	0.0436	0.0076	0.0858	0.8948	Random Forest Regressor	36.96	5942	73.85	0.9622
Decision Tree Regressor	0.0551	0.0115	0.1029	0.8516	K Neighbors Regressor	61.76	9733	97.38	0.9356
K Neighbors Regressor	0.0669	0.0188	0.1326	0.7638	Decision Tree Regressor	57.40	11,441	104.4	0.9243
AdaBoost Regressor	0.1143	0.0190	0.1372	0.7271	AdaBoost Regressor	91.63	13,579	115.1	0.9092
Bayesian Ridge	0.1393	0.0378	0.1921	0.4875	Ridge Regression	93.21	16,431	126.8	0.8926
Ridge Regression	0.1395	0.0378	0.1921	0.4871	Bayesian Ridge	93.27	16,431	126.8	0.8926
Linear Regression	0.1396	0.0378	0.1921	0.4869	Lasso Regression	92.97	16,433	126.8	0.8926
Least Angle Regression	0.1396	0.0378	0.1921	0.4869	Linear Regression	93.33	16,431	126.8	0.8925
Huber Regressor	0.1221	0.0456	0.2084	0.4194	Least Angle Regression	93.33	16,431	126.8	0.8925
Orthogonal Matching Pursuit	0.1579	0.0494	0.2197	0.3281	Huber Regressor	87.91	18,109	132.1	0.8833
Passive Aggressive Regressor	0.1706	0.0593	0.2354	0.2287	Passive Aggressive Regressor	88.70	18,674	134.1	0.8799
Lasso Regression	0.1989	0.0773	0.2737	-0.0175	Lasso Least Angle Regression	91.54	18,862	135.1	0.8778
Elastic Net	0.1989	0.0773	0.2737	-0.0175	Orthogonal Matching Pursuit	109.7	24,850	155.5	0.8370
Lasso Least Angle Regression	0.1989	0.0773	0.2737	-0.0175	Elastic Net	129.5	32,665	178.7	0.7873
Dummy Regressor	0.1989	0.0773	0.2737	-0.0175	Dummy Regressor	322.3	153,789	390.9	-0.024

 $R^2$ 

RMSE

plots were obtained using a 10-fold cross-validation method, where the  $\rm R^2$  values are averaged across the 10-fold runs. The predictability of the chosen surrogate models was examined using the validation data. As can be seen in Fig. 6(a) and (d), generally accurate predictions are obtained for recovery and power consumption. On the other hand, in Fig. 6(b) and (d), there are samples with significant errors for purity in the lower range, and for BSF in the higher range. However, these were deemed acceptable; operating conditions that give such low purity or high BSF are unpractical and not employed in this study. The  $\rm R_2$  value of 0.9099 for purity is relatively low, which is due to the narrow range of purity which consistently exceeds 98 % because of the very high selectivity of ELM-11. The predictability of the surrogate models was further tested

using four different points on the Pareto front, as shown in Section 4.2.

#### 4.2. Multi-objective optimization

The surrogate models formulated in the previous section are used for multi-objective optimization here. The Pareto-optimal solutions obtained from our multi-objective optimization formulation given in Eq. (22), using the non-dominated sorting genetic algorithm II (NSGA-II) solver in the Optuna package, are visualized in Fig. 7. This exploration, conducted over a population of 10,000 points, yielded results that were subsequently plotted in two dimensions.

Some distinctive trends can also be seen in the Pareto fronts in Fig. 7,

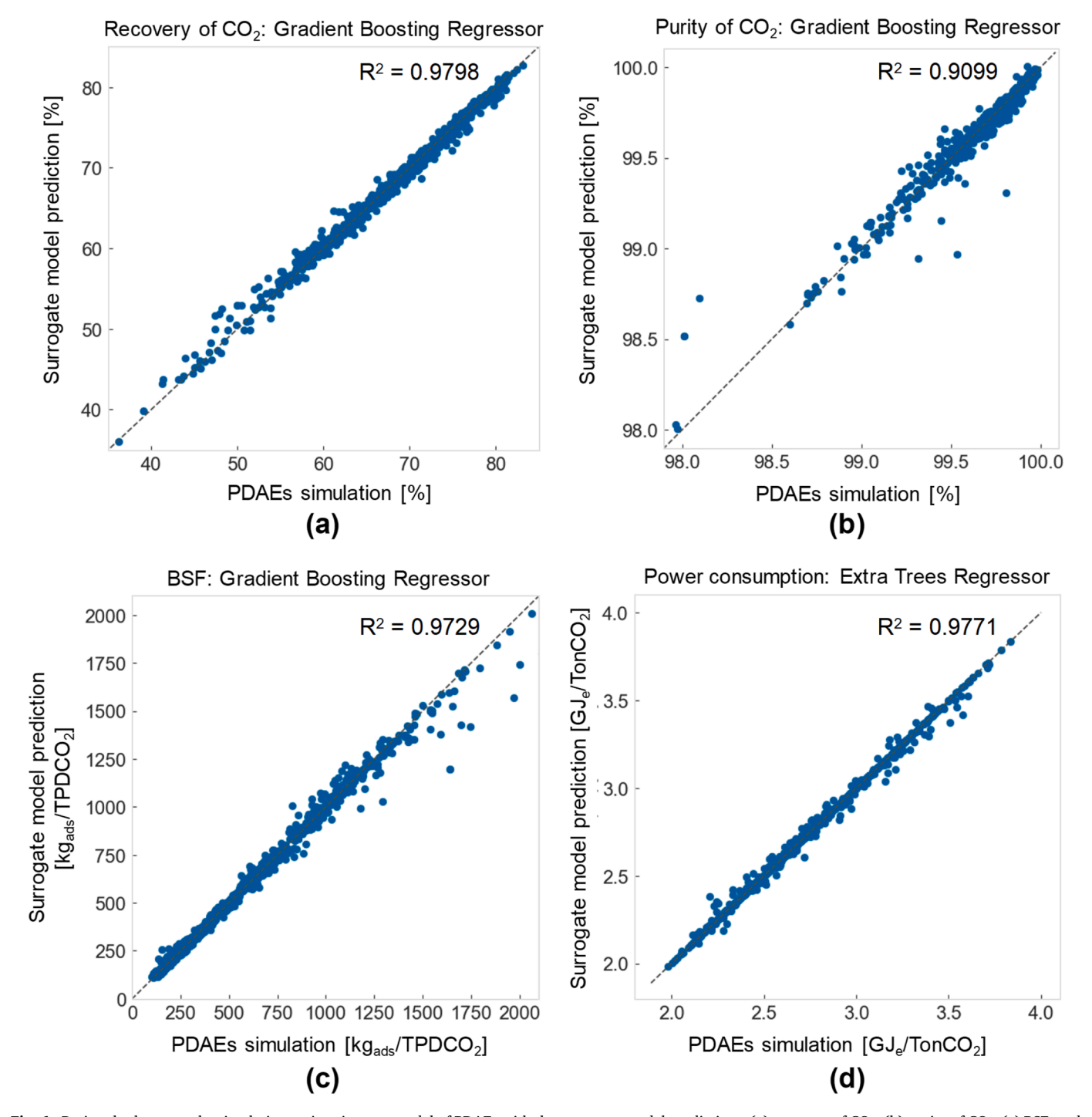


Fig. 6. Parity plot between the simulations using rigorous model of PDAEs with the surrogate model predictions: (a) recovery of CO<sub>2</sub>; (b) purity of CO<sub>2</sub>; (c) BSF; and (d) power consumption.

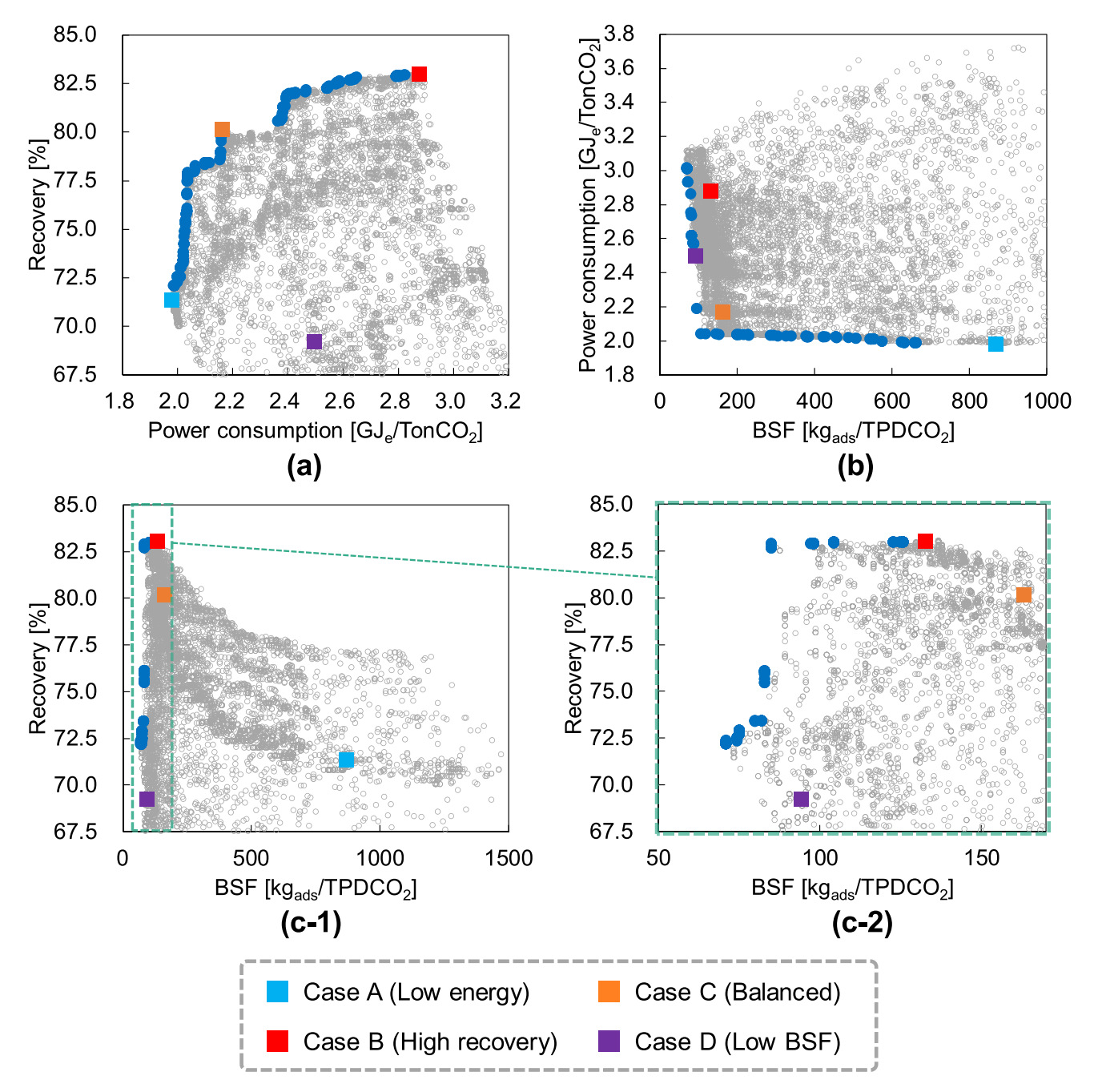


Fig. 7. The Pareto-optimal solutions of the multi-objective optimization problem: (a) Power consumption vs. recovery; (b) BSF vs. power consumption; (c-1) BSF vs. recovery; (c-2) zoomed BSF vs. recovery.

which cannot be seen in adsorption processes using conventional adsorbents. In Fig. 7(b) where the power consumption is plotted against BSF, an "elbow" can be seen in the Pareto front. This indicates that when we try to save the power consumption below a critical value of approximately 2.0  $\rm GJ_e/TPDCO_2$ , the BSF increases significantly. Furthermore, in Fig. 7(c-1), the Pareto front of recovery is nearly vertical. These trends are due to the sigmoidal shape of the isotherm of ELM-11, where the uptake increase sharply once the pressure exceeds the gate pressure (Fig. 1).

Specifically, we highlight four exemplary points within these Pareto solutions, which we have denoted as Cases A through D. Table 6 presents the results of validating the surrogate predictions against simulations for Cases A through D. The errors between estimation and simulation are sufficiently small (< 5.17%) except for Case D of BSF. The reasons for

the relatively large errors of over 5 % for BSF Cases D are as follows: first, unlike other performance indicators, BSF has a wide range of 90–900 kg<sub>ads</sub>/TPDCO<sub>2</sub>, where Cases A and D are near the maximum and minimum of the BSF, respectively. A specific cause for the relatively large error of -12.8 % shown by Case D is because of Eq. (20): which was implemented to enable computational convergence of the PDAEs. The max function in Eq. (20) introduces nonlinearity and non-smoothness when the desorption times becomes shorter than 150 s, i.e., when BSF is small, such as Case D, non-negligible error is observed between estimation and simulation. However, when the desorption time exceeds 150 s, as in Cases A-C, the function does not affect BSF.

Each of Cases A through D exhibits distinctive operating strategies. Case A minimizes power consumption by maintaining low feed pressure ( $P_{\text{feed}} = 719.1 \text{ [kPa]}$ ) while employing the high desorption pressure ( $C_{\text{des}}$ )

**Table 6**Comparison among the cases A–D.

A (Low energy)	B (High recovery)	C (Balanced)	D (Low BSF)	
719.1	1494	847.4	874.0	
273.2	273.3	273.3	292.0	
1.114	1.257	1.233	1.643	
0.523	0.2010	0.2070	0.2107	
ions from sim	ulation			
12.73	4.896	4.970	9.639	
0.3984	0.2372	0.2394	0.3488	
280	410	350	320	
3800	650	700	150	
nparison				
71.33	83.03	80.17	69.20	
72.01	84.61	81.10	67.56	
-0.956	-1.91	-1.16	2.36	
1.982	2.878	2.165	2.497	
1.984	2.875	2.261	2.496	
-0.0787	0.133	-4.45	0.069	
868.5	132.8	163.2	94.3	
823.6	131.8	161.9	106.4	
5.17	0.764	0.803	-12.8	
99.65 99.61 0.0399	99.97 99.96 0.0126	99.80 99.89 0.0901	99.85 99.87 -0.0115	
	energy)  719.1 273.2 1.114 0.523 tions from sim 12.73 0.3984 280 3800 nparison 71.33 72.01 -0.956 1.982  1.984 -0.0787 868.5 823.6 5.17 99.65 99.61	energy) recovery)  719.1 1494 273.2 273.3 1.114 1.257 0.523 0.2010 citons from simulation 12.73 4.896 0.3984 0.2372 280 410 3800 650  mparison 71.33 83.03 72.01 84.61 -0.956 -1.91 1.982 2.878  1.984 2.875  -0.0787 0.133 868.5 132.8 823.6 131.8 5.17 0.764 99.65 99.97 99.61 99.96	energy) recovery) (Balanced)  719.1 1494 847.4 273.2 273.3 273.3 1.114 1.257 1.233 0.523 0.2010 0.2070 citons from simulation 12.73 4.896 4.970 0.3984 0.2372 0.2394 280 410 350 3800 650 700  mparison 71.33 83.03 80.17 72.01 84.61 81.10 -0.956 -1.91 -1.16 1.982 2.878 2.165  1.984 2.875 2.261  -0.0787 0.133 -4.45 868.5 132.8 163.2 823.6 131.8 161.9 5.17 0.764 0.803 99.65 99.97 99.80 99.61 99.96 99.89	

= 0.523 [-], resulting in  $P_{des}$  = 12.73 [kPa]). As seen in Table 6, which outlines other operating conditions from simulations, Case A shows a higher  $C_{des}$  compared to the other cases, conserving the energy of the vacuum pump. However, setting a high Cdes results in an increased desorption time ( $t_{des} = 3800$  [s]), leading to the highest BSF among all cases, at 823.6 kg<sub>ads</sub>/TPDCO<sub>2</sub>. On the other hand, Case B maximizes recovery; by setting the  $P_{\rm feed}$  near its upper limit of 1500 kPa and the  $T_{\text{wall}}$  and  $C_{\text{des}}$  close to their respective lower limits of 273 K and 0.200, this case shows the highest recovery of 84.61 [%]. However, power consumption is relatively high at 2.878 GJ<sub>e</sub>/tonneCO<sub>2</sub>. Case C balances power consumption and recovery; as in Case B, by setting  $T_{\text{wall}}$  and  $C_{\text{des}}$ near the lower limit while setting  $P_{\text{high}}$  to a medium value 847.4 kPa, high recovery of 80.17 % and low power consumption of 2.165 GJ<sub>e</sub>/ TPDCO<sub>2</sub> are achieved. Finally, Case D is a scenario where BSF is low. In this case, by setting  $T_{\text{wall}}$  to a relatively high value of 292.0 K and keeping  $C_{\text{des}}$  low at 0.2107, desorption time is reduced to 150 s. This reduction in cycle time contributes to the reduction of BSF.

The recovery is <80% in many cases due to the slipping-off problem common in flexible MOFs, where  $CO_2$  below the gate pressure tends to slip through, resulting in lower recovery. One way to address this issue is to use the flexible MOF with another adsorbent in series (Hiraide et al., 2020). However, this paper investigates the achievable recovery for the single-column VPSA process using ELM-11.

### 5. Conclusion

In this study, we carried out multi-objective optimization analysis for a unique adsorbent, Elastic Layer-structured Metal-organic Framework-11 (ELM-11), in a Vacuum Pressure Swing Adsorption (VPSA) process. This is the first study to investigate the optimal performance of a VPSA process using a flexible MOF. To handle the complex characteristics of ELM-11 such as sigmoidal isotherms with hysteresis that pose considerable challenges in dynamic simulation and optimization, we employed

a state-of-the-art optimization technique using Automated Machine Learning (AutoML) and surrogate model optimization, which allowed us to identify optimal operations for the four objective functions: purity, recovery, bed size factor (BSF), and power consumption. The trade-offs of the four objective functions of the flexible MOF were analyzed carefully.

Our surrogate model, which was found to give the highest prediction accuracy from 18 candidates, enabled us to examine the impacts of four decision variables on the performance indicators of the VPSA process. This investigation facilitated understanding of the relationship between operating parameters (decision variables) and performance indicators.

Distinct trends of the VPSA process using ELM-11 were found in the analysis using Shapley Additive Explanations (SHAP). Unlike the conventional VPSA processes where the purity is highly influenced by the feed volume amount, the  $\rm CO_2$  purity of our process remains always high, owing to the high selectivity of ELM-11. Furthermore, it was found that the column wall temperature and feed pressure have the most significant impact on recovery, and reducing desorption pressure can increase the recovery rate by up to 8 %.

Optimal operating conditions were identified through multiobjective optimization. The surrogate model was validated against the rigorous model at four exemplary points on the Pareto front. However, some errors were identified, particularly in the Bed Size Factor (BSF) ranging in an order of magnitude, which can be a subject in a future study. While this study considered single-stage compression, it is worth noting that multi-stage compression can potentially reduce the power consumption. Furthermore, as demonstrated in the study by Hiraide et al. (2020), combining multiple adsorbents can lower the pressure, thereby further reducing power consumption.

The application of a surrogate model-based optimization for the VPSA process is an effective and computationally efficient approach to design a  $\rm CO_2$  capture system using an adsorbent with sigmoidal isotherm shapes with hysteresis. Some issues are left for future work, such as investigations into the capabilities of other flexible MOFs in adsorption processes.

# CRediT authorship contribution statement

Yuya Takakura: Formal analysis, Investigation, Methodology, Validation, Visualization, Writing – original draft. Suryateja Ravutla: Formal analysis, Methodology, Supervision, Writing – review & editing. Jinsu Kim: Formal analysis, Methodology, Supervision, Writing – review & editing. Keisuke Ikeda: Data curation, Formal analysis, Investigation, Software. Hiroshi Kajiro: Conceptualization, Funding acquisition, Resources, Supervision. Tomoyuki Yajima: Project administration, Supervision, Junpei Fujiki: Project administration, Supervision, Writing – review & editing. Fani Boukouvala: Conceptualization, Methodology, Project administration, Resources, Supervision, Writing – review & editing. Matthew Realff: Conceptualization, Methodology, Project administration, Resources, Supervision, Writing – review & editing. Yoshiaki Kawajiri: Conceptualization, Funding acquisition, Project administration, Supervision, Writing – review & editing.

#### Declaration of competing interest

The authors declare the following financial interests/personal relationships which may be considered as potential competing interests:

Yoshiaki Kawajiri reports financial support was provided by Nippon Steel Corporation. Yuya Takakura reports financial support was provided by Hoshizaki Scholarship. Yuya Takakura reports financial support was provided by Nitto Foundation. Yoshiaki Kawajiri has patent #2022–182,180 pending to Japan Patent Office. If there are other authors, they declare that they have no known competing financial interests or personal relationships that could have appeared to influence the work reported in this paper.

#### Acknowledgments

We gratefully acknowledge the financial support provided by Nippon Steel Corporation. Yuya Takakura was sponsored by Hoshizaki Scholarship, and the Nitto Foundation.

#### Supplementary materials

Supplementary material associated with this article can be found, in the online version, at doi:10.1016/j.ijggc.2024.104260.

#### References

- Aaron, D., Tsouris, C., 2005. Separation of  $CO_2$  from flue gas: a review. Sep. Sci. Technol. 40, 321–348. https://doi.org/10.1081/SS-200042244.
- Agarwal, A., Biegler, L.T., Zitney, S.E., 2009. Simulation and optimization of pressure swing adsorption systems using reduced-order modeling. Ind. Eng. Chem. Res. 48, 2327–2343. https://doi.org/10.1021/ie071416p.
- Akiba, T., Sano, S., Yanase, T., Ohta, T., Koyama, M., 2019. Optuna: a next-generation hyperparameter optimization framework. In: Proceedings of the 25th ACM SIGKDD International Conference on Knowledge Discovery & Data Mining, pp. 2623–2631. https://doi.org/10.48550/arXiv.1907.10902.
- Barton, P.I., Pantelides, C.C., 1994. Modeling of combined discrete/continuous processes. AIChE J. 40, 966–979. https://doi.org/10.1002/aic.690400608.
- Beck, J., Friedrich, D., Brandani, S., Fraga, E.S., 2015. Multi-objective optimisation using surrogate models for the design of VPSA systems. Comput. Chem. Eng. 82, 318–329. https://doi.org/10.1016/j.compchemeng.2015.07.009.
- Bon, V., Kavoosi, N., Senkovska, I., Kaskel, S., 2015. Tolerance of flexible MOFs toward repeated adsorption stress. ACS Appl. Mater. Interfaces 7, 22292–22300. https://doi. org/10.1021/acsami.5b05456.
- Bon, V., Senkovska, I., Wallacher, D., Heerwig, A., Klein, N., Zizak, I., Feyerherm, R., Dudzik, E., Kaskel, S., 2014. *In situ* monitoring of structural changes during the adsorption on flexible porous coordination polymers by X-ray powder diffraction: instrumentation and experimental results. Microporous Mesoporous Mater. 188, 190–195. https://doi.org/10.1016/j.micromeso.2013.12.024.
- Coudert, F.X., Boutin, A., Fuchs, A.H., Neimark, A.V., 2013. Adsorption deformation and structural transitions in metal–organic frameworks: from the unit cell to the crystal. J. Phys. Chem. Lett. 4, 3198–3205. https://doi.org/10.1021/jz4013849.
- Diwekar, U.M., Kalagnanam, J.R., 1997. Efficient sampling technique for optimization under uncertainty. AIChE J. 43, 440–447. https://doi.org/10.1002/aic.690430217
- Fujiki, J., Kajiro, H., Takakura, Y., Yajima, T., Kawajiri, Y., 2023. Breakthrough analysis for parameter estimation of CO<sub>2</sub> adsorption on pelletized flexible metal-organic framework. Chem. Eng. J. 460, 141781. https://doi.org/10.1016/j. cpi 2023 141781
- Hao, Z., Caspari, A., Schweidtmann, A.M., Vaupel, Y., Lapkin, A.A., Mhamdi, A., 2021. Efficient hybrid multiobjective optimization of pressure swing adsorption. Chem. Eng. J. 423, 130248. https://doi.org/10.1016/j.cej.2021.130248.
- Hefti, M., Joss, L., Bjelobrk, Z., Mazzotti, M., 2016. On the potential of phase-change adsorbents for CO<sub>2</sub> capture by temperature swing adsorption. Faraday Discuss. 192, 153–179. https://doi.org/10.1039/C6FD00040A.
- Hiraide, S., Sakanaka, Y., Kajiro, H., Kawaguchi, S., Miyahara, M.T., Tanaka, H., 2020. High-throughput gas separation by flexible metal-organic frameworks with fast gating and thermal management capabilities. Nat. Commun. 11, 3867. https://doi. org/10.1038/s41467-020-17625-3.
- Hiraide, S., Tanaka, H., Ishikawa, N., Miyahara, M.T., 2017. Intrinsic thermal management capabilities of flexible metal–organic frameworks for carbon dioxide separation and capture. ACS Appl. Mater. Interfaces. 9, 41066–41077. https://doi. org/10.1021/acsami.7b13771.
- Hiraide, S., Tanaka, H., Miyahara, M.T., 2016. Understanding gate adsorption behaviour of CO<sub>2</sub> on elastic layer-structured metal-organic framework-11. Dalton Trans. 45, 4193–4202. https://doi.org/10.1039/C5DT03476K.
- Horike, S., Shimomura, S., Kitagawa, S., 2009. Soft porous crystals. Nat. Chem. 1, 695–704. https://doi.org/10.1038/nchem.444.
- James, S.L., 2003. Metal-organic frameworks. Chem. Soc. Rev. 32, 276. https://doi.org/ 10.1039/b200393g.
- Kim, J., Son, M., Sup Han, S., Yoon, Y.S., Oh, H., 2022a. Computational-cost-efficient surrogate model of vacuum pressure swing adsorption for CO separation process optimization. Sep. Purif. Technol. 300, 121827. https://doi.org/10.1016/j. sepur. 2022 121827
- Kim, S.H., Landa, H.O.R., Ravutla, S., Realff, M.J., Boukouvala, F., 2022b. Data-driven simultaneous process optimization and adsorbent selection for vacuum pressure swing adsorption. Chem. Eng. Res. Des. 188, 1013–1028. https://doi.org/10.1016/j. cherd.2022.10.002.
- Ko, D., Siriwardane, R., Biegler, L.T., 2005. Optimization of pressure swing adsorption and fractionated vacuum pressure swing adsorption processes for CO<sub>2</sub> capture. Ind. Eng. Chem. Res. 44, 8084–8094. https://doi.org/10.1021/ie050012z.
- Kondo, A., Noguchi, H., Ohnishi, S., Kajiro, H., Tohdoh, A., Hattori, Y., Xu, W.C., Tanaka, H., Kanoh, H., Kaneko, K., 2006. Novel expansion/shrinkage modulation of 2D layered MOF triggered by clathrate formation with CO<sub>2</sub> molecules. Nano Lett. 6, 2581–2584. https://doi.org/10.1021/nl062032b.

- Kultaeva, A., Bon, V., Weiss, M.S., Pöppl, A., Kaskel, S., 2018. Elucidating the formation and transformation mechanisms of the switchable metal–organic framework ELM-11 by powder and single-crystal EPR study. Inorg. Chem. 57, 11920–11929. https://doi. org/10.1021/acs.inorgchem.8b01241.
- Leperi, K.T., Yancy-Caballero, D., Snurr, R.Q., You, F., 2019. 110th Anniversary: surrogate models based on artificial neural networks to simulate and optimize pressure swing adsorption cycles for  $\rm CO_2$  capture. Ind. Eng. Chem. Res. 58, 18241-18252. https://doi.org/10.1021/acs.iecr.9b02383.
- Li, D., Kaneko, K., 2001. Hydrogen bond-regulated microporous nature of copper complex-assembled microcrystals. Chem. Phys. Lett. 335, 50–56. https://doi.org/ 10.1016/S0009-2614(00)01419-6.
- Lundberg, S.M., Erion, G., Chen, H., DeGrave, A., Prutkin, J.M., Nair, B., Katz, R., Himmelfarb, J., Bansal, N., Lee, S.I., 2020. From local explanations to global understanding with explainable AI for trees. Nat. Mach. Intell. 2, 56–67. https://doi. org/10.1038/s42256-019-0138-9.
- Majchrzak-Kucęba, I., Wawrzyńczak, D., Ściubidło, A., 2019. Application of metalorganic frameworks in VPSA technology for CO<sub>2</sub> capture. Fuel 255, 115773. https:// doi.org/10.1016/j.fuel.2019.115773.
- Mason, J.A., Oktawiec, J., Taylor, M.K., Hudson, M.R., Rodriguez, J., Bachman, J.E., Gonzalez, M.I., Cervellino, A., Guagliardi, A., Brown, C.M., Llewellyn, P.L., Masciocchi, N., Long, J.R., 2015. Methane storage in flexible metal–organic frameworks with intrinsic thermal management. Nature 527, 357–361. https://doi.org/10.1038/nature15732.
- Pai, K.N., Prasad, V., Rajendran, A., 2020. Experimentally validated machine learning frameworks for accelerated prediction of cyclic steady state and optimization of pressure swing adsorption processes. Sep. Purif. Technol. 241, 116651. https://doi. org/10.1016/j.seppur.2020.116651.
- Peszyńska, M., Showalter, R.E., 1998. A transport model with adsorption hysteresis. Differ. Integral Equ. 11, 327–340. https://doi.org/10.57262/die/1367341074.
- Sant Anna, H.R., Barreto, A.G., Tavares, F.W., de Souza, M.B., 2017. Machine learning model and optimization of a PSA unit for methane-nitrogen separation. Comput. Chem. Eng. 104, 377–391. https://doi.org/10.1016/j.compchemeng.2017.05.006.
- Schneemann, A., Bon, V., Schwedler, I., Senkovska, I., Kaskel, S., Fischer, R.A., 2014. Flexible metal-organic frameworks. Chem. Soc. Rev. 43, 6062–6096. https://doi.org/10.1039/C4CS00101J.
- Shen, C., Liu, Z., Li, P., Yu, J., 2012. Two-stage VPSA process for CO<sub>2</sub> capture from flue gas using activated carbon beads. Ind. Eng. Chem. Res. 51, 5011–5021. https://doi. org/10.1021/ie202097v.
- Shen, C., Yu, J., Li, P., Grande, C.A., Rodrigues, A.E., 2011. Capture of CO<sub>2</sub> from flue gas by vacuum pressure swing adsorption using activated carbon beads. Adsorption 17, 179–188. https://doi.org/10.1007/s10450-010-9298-v.
- Subraveti, S.G., Li, Z., Prasad, V., Rajendran, A., 2019. Machine learning-based multiobjective optimization of pressure swing adsorption. Ind. Eng. Chem. Res. 58, 20412–20422. https://doi.org/10.1021/acs.iecr.9b04173.
- Sugimoto, S., Takakura, Y., Kajiro, H., Fujiki, J., Dashti, H., Yajima, T., Kawajiri, Y., 2023. Modeling, parameter estimation, and uncertainty quantification for CO<sub>2</sub> adsorption process using flexible metal-organic frameworks by Bayesian Monte Carlo methods. J. Adv. Manuf. Process. 5, e10165. https://doi.org/10.1002/psp. 2016.
- Takakura, Y., Sugimoto, S., Fujiki, J., Kajiro, H., Yajima, T., Kawajiri, Y., 2022. Model-based analysis of a highly efficient CO<sub>2</sub> separation process using flexible metal–organic frameworks with isotherm hysteresis. ACS Sustain. Chem. Eng. 10, 14935–14947. https://doi.org/10.1021/acssuschemeng.2c05058.
- Tanaka, H., Hiraide, S., Kondo, A., Miyahara, M.T., 2015. Modeling and visualization of CO<sub>2</sub> adsorption on elastic layer-structured metal-organic framework-11: toward a better understanding of gate adsorption behavior. J. Phys. Chem. C 119, 11533–11543. https://doi.org/10.1021/jp512870p.
   Tong L., Bénard P., Zong Y., Chahine R., Liu K., Xiao J., 2021. Artificial neural network
- Tong L., Bénard P., Zong Y., Chahine R., Liu K., Xiao J., 2021. Artificial neural network based optimization of a six-step two-bed pressure swing adsorption system for hydrogen purification. Energy and AI 5, 100075. 10.1016/j.egyai.2021.100075.
- Vo, N.D., Oh, D.H., Kang, J.H., Oh, M., Lee, C.H., 2020. Dynamic-model-based artificial neural network for H<sub>2</sub> recovery and CO<sub>2</sub> capture from hydrogen tail gas. Appl. Energy 273, 115263. https://doi.org/10.1016/j.apenergy.2020.115263.
- Xiao, J., Li, C., Fang, L., Böwer, P., Wark, M., Bénard, P., Chahine, R., 2020. Machine learning-based optimization for hydrogen purification performance of layered bed pressure swing adsorption. Int. J. Energy Res. 44, 4475–4492. https://doi.org/ 10.1002/er.5225.
- Xu, M., Chen, S., Seo, D.K., Deng, S., 2019. Evaluation and optimization of VPSA processes with nanostructured zeolite NaX for post-combustion CO<sub>2</sub> capture. Chem. Eng. J. 371, 693–705. https://doi.org/10.1016/j.cej.2019.03.275.
- Yang, J., Yu, Q., Zhao, Q., Liang, J., Dong, J., Li, J., 2012. Adsorption CO<sub>2</sub>, CH<sub>4</sub> and N<sub>2</sub> on two different spacing flexible layer MOFs. Microporous Mesoporous Mater. 161, 154–159. https://doi.org/10.1016/j.micromeso.2012.01.008.
- Ye, F., Ma, S., Tong, L., Xiao, J., Bénard, P., Chahine, R., 2019. Artificial neural network based optimization for hydrogen purification performance of pressure swing adsorption. Int. J. Hydrog. Energy 44, 5334–5344. https://doi.org/10.1016/j. iihydene.2018.08.104.
- Yu, X., Shen, Y., Guan, Z., Zhang, D., Tang, Z., Li, W., 2021. Multi-objective optimization of ANN-based PSA model for hydrogen purification from steam-methane reforming gas. Int. J. Hydrog. Energy 46, 11740–11755. https://doi.org/10.1016/j. ijhydene.2021.01.107.
- Zhou, H.C., Kitagawa, S., 2014. Metal-organic frameworks (MOFs). Chem. Soc. Rev. 43, 5415–5418. https://doi.org/10.1039/C4CS90059F.